Int. J. Electrochem. Sci., 15 **(2020)** 7601 – 7609, doi: 10.20964/2020.08.09

International Journal of
ELECTROCHEMICAL
SCIENCE
www.electrochemsci.org

Short Communication

Preparation and Capacitance Properties of Dumbbell-Shaped Mn_2O_3 Mesocrystal as High-Performance Supercapacitors

Guiling Wang[1,], Qiannan Li[1], Mengyu Du[1], Junming Chen[1], Tingting Liu[2], Xinyu Wang[1], Weimin Zhang[1], Xuchun Wang[1]*

[1] College of Chemical and Materials Engineering, Anhui Science and Technology University, Donghua Road No. 9, Fengyang, 233100, China;
[2] Northeast Petroleum University at Qinhuangdao, Qinhuangdao 066004, China)
[*]E-mail: wangguilingcg@126.com

Received: 16 October 2019 / *Accepted:* 17 April 2020 / *Published:* 10 July 2020

Dumbbell-shaped Mn_2O_3 was synthesized by annealing hydrothermal products with a precisely controlled concentration of ethanol. When the ratio of ethanol increased, various Mn_2O_3 nanostructures with different morphologies, ranging from a dumbbell-like shape to a spherical shape, were obtained. Dumbbell-like Mn_2O_3 had a mesocrystal structure, which was formed by an orderly stacking of nanocrystallites. In addition, with a water to ethanol volume ratio of 1:1, Mn_2O_3 exhibited the highest specific capacitance of 273.1 F g^{-1} at a current density of 1 A g^{-1} in 6 M KOH electrolyte and a good capacitance retention of 97.7% after 1000 cycles. Furthermore, the noninsertion and insertion capacities of the sample materials were further analysed. The total maximum capacitance and the minimum capacitance were calculated to be 411.5 F g^{-1} and 230.5 F g^{-1}, respectively; moreover, it could be calculated that the insertion capacity percentage was 44%. This work provides new innovative insights to improve the capacitance performance of a Mn_2O_3 material by optimizing the crystal structure.

Keywords: supercapacitor; Mn_2O_3; dumbbell-like shape; mesocrystal; electrochemical performance

1. INTRODUCTION

Supercapacitors have attracted considerable attention worldwide due to their high power density, long cycling life and fast recharge ability; thus, supercapacitors can fill the gap between conventional capacitors and batteries [1-3]. From a material point of view, manganese oxides are one of the most attractive materials because of their high theoretical specific capacitance (1370 F g^{-1} as the oxidation state of Mn ion changes from +4 to +3 over a potential window of 0.8 V) [4], low cost due to their natural abundance, and their environmental friendliness. Among various manganese oxide materials (MnO_2, Mn_2O_3 Mn_3O_4, MnO, *etc.*), MnO_2-based materials [5-10] are usually studied as supercapacitor materials

at this stage. However, crystalline Mn_2O_3 is generally known as electrochemically inactive in aqueous cells. Therefore, pure Mn_2O_3 materials have rarely been reported as supercapacitors; moreover, even if they are reported, the reported properties in the articles are unsatisfactory. For example, Lee [11] et al prepared Mn_2O_3 nanowires, obtaining a specific capacitance of 69 F g^{-1} at a scan rate of 10 mV s^{-1}. Li [12] et al synthesized a porous Mn_2O_3 nanocubic structure that exhibited a specific capacitance of 191.1 F g^{-1} at a current density of 0.1 A g^{-1}. Moreover, Li [13] et al synthesized Mn_2O_3 nanowalls (with an average wall thickness of only 20–30 nm) on nickel (Ni) foam by a facile hydrothermal route. The composite presented a specific capacitance of 461 F g^{-1} at a current density of 0.5 A g^{-1} and retained 82% of its initial capacitance after 5000 cycles.

Currently, the application of nanostructure materials has become a global research hot spot in various application fields. However, they have the following limitations as supercapacitor materials. First, they easily agglomerate, which reduces the surface area and decreases the amount of full contact with the electrolyte. Moreover, bare nanostructure materials exhibit a low capacitance retention due to their low mechanical stability poorly accommodating the large volume change that occurs during the charge and discharge process. Compared with nanostructure materials, mesocrystals, a kind of porous material assembled by nanoscale crystallites with a common orientation, possess improved electrochemical performance due to their nanoparticle size and long-range electronic connectivity, structural coherence and mesocrystal porosity [14-16]. Recently, Yang [17] et al synthesized self-assembled α-Fe_2O_3 mesocrystals/graphene nanohybrids, which showed a unique mesocrystal porous structure, large specific surface area, and high conductivity. This unique architecture delivered an enhanced capacitance. Bi et al. [18] prepared mesocrystal nanosheets of vanadium nitride as a supercapacitor material. This mesocrystal displayed an electrical conductivity of 1.44×10^5 S m^{-1} and exhibited a superior volumetric capacitance of 1937 mF cm^{-3}. Hou et al. [19] prepared two-dimensional ultra-thin α-$Co(OH)_2$ mesocrystal nanosheets; this unique structure presented excellent properties as an electrochemical capacitor. However, manganese oxide mesocrystals as supercapacitor materials have not been reported.

Herein, we report a method to prepare mesocrystal Mn_2O_3 by a thermal decomposition of a $MnCO_3$ precursor. Importantly, the obtained mesocrystal Mn_2O_3 with a dumbbell-like shape shows outstanding electrochemical performance when applied as a supercapacitor electrode material.

2. EXPERIMENTAL

2.1 Material synthesis

$KMnO_4$ and glucose were mixed in 50 mL of a water-ethanol solution. The volume ratios between the water and ethanol in the solutions were 5:0, 4:1, 3:2, 1:1, 2:3 and 1:4, and the corresponding samples were named V_{50}, V_{40}, V_{30}, V_{25}, V_{20} and V_{10}, respectively, in this work. Subsequently, each of the solution mixtures was stirred with a magnetic stirrer for 10 min to yield a homogenous solution at room temperature. Next, the solution was transferred to a Teflon-lined stainless steel autoclave with a 100-ml capacity, which was then loaded into an oven to react at 180 °C for 12 h. Thereafter, the pressure

vessel was cooled by natural convection. The precipitates were filtered and washed using deionized water and dried in a vacuum oven at 80 °C overnight to form $MnCO_3$. Mn_2O_3 was prepared by heating the $MnCO_3$ precursor at 400 °C for 4 h in an air atmosphere.

2.2 Materials Characterization

The crystal structures of the samples were characterized by X-ray diffraction (XRD, Rigaku d/MAX-2500/pc) with Cu Kα radiation, λ=1.54056 Å. Field-emission scanning electron microscopy (FE-SEM) images of the as-synthesized products were measured with scanning electron microscopy (SEM, S-4800 operated at 10 kV). TEM and selected area electron diffraction (SAED) analyses were obtained with high-resolution transmission electron microscopy (HR-TEM, JEM2010). Moreover, the samples were also characterized by the BET method with a NOVA 4000e surface area and size analyser. The electrical conductivity was measured by a powder resistivity measuring instrument (ST2722-SZ).

2.3 Electrochemical Measurement

The working electrodes consisted of 80 *wt.*% activated material, 15 *wt.*% acetylene black and 5 *wt.*% PTFE (60 *wt.*% suspension in water). The viscous slurry consisting of the above mixture was smeared on a foam nickel mesh with an area of 1 cm × 1 cm. Next, the sample was dried in vacuum at 80 °C for 12 h, and then they were pressed at 2 MPa for 10 min to obtain better contact. The mass loading of each electrode was approximately 3 mg. The counter electrode was prepared from a mixture of activated carbon, acetylene blank and PTFE in a weight ratio of 80:15:5. The slurry was smeared onto a nickel foam with an area of 2.5 cm × 2.5 cm.

Electrochemical investigations were carried out with a three-electrode system using Hg/HgO as the reference electrode and 6 M KOH as the electrolyte. Cyclic voltammetry (CV) studies were performed in a potential range of -0.1~0.55 V (*vs.* Hg/HgO) at different scan rates. CV tests were conducted with a CHI660E electrochemical workstation (Chenhua, Shanghai, China). Galvanostatic charge-discharge experiments were conducted using computer-controlled cycling equipment (NEWARE, Shenzhen, China).

3. RESULTS AND DISCUSSION

3.1 Morphological and structural analysis

The as-formed Mn_2O_3 products were characterized by XRD, SEM and TEM. Figure 1 shows the XRD patterns of Mn_2O_3 prepared in solvents with different compositions. All peaks can be indexed to the cubic phase bixbyite (JCPDS No. 10-0069). It is obvious that the related peak intensity becomes weaker with decreasing water content, and the peaks become inconspicuous when the volume ratio reaches 1:4. This phenomenon demonstrates that the long-range order structure of Mn_2O_3 becomes poorer with decreasing water content.

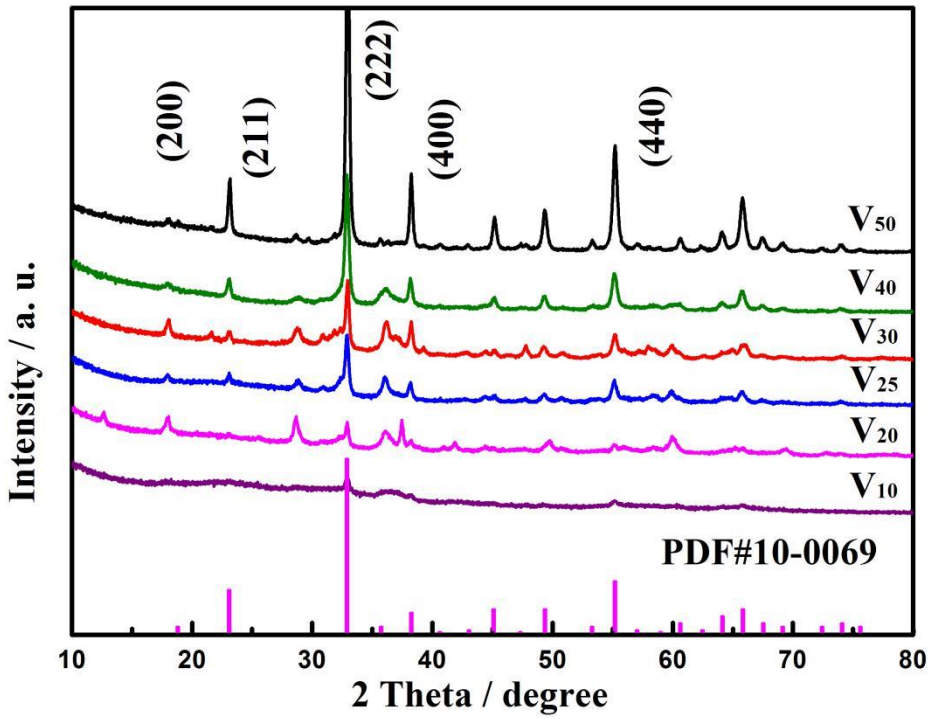

Figure 1. XRD patterns of different Mn_2O_3 powders prepared in solvents with different compositions.

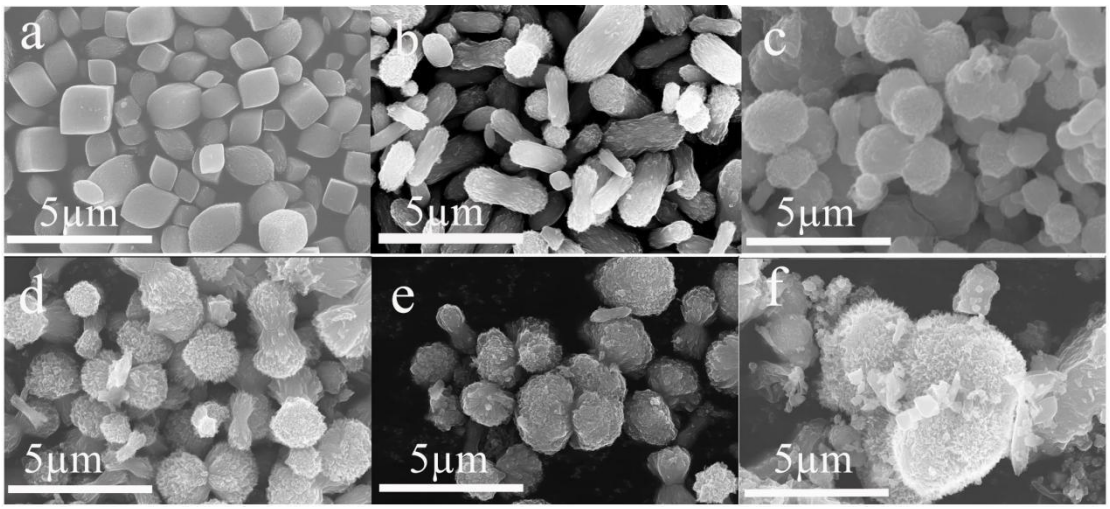

Figure 2. SEM images of Mn_2O_3 powders prepared in solvents with different compositions a) V_{50}, b) V_{40}, c) V_{30}, d) V_{25}, e) V_{20}, and f) V_{10}.

The morphology of the Mn_2O_3 samples is presented in Figure 2. It can be seen from the figure that the shape of the sample transforms from a diamond to a dumbbell as the ratio of water to ethanol increases from V_{50} to V_{25}. Additionally, the SEM image shows that most of the V_{25} particles (Figure 2d)

present a dumbbell-like shape with a length of a few micrometres. With a further increase in ethanol, the samples gradually expand until they become spherical when the ratio between water and ethanol reaches 1:4 (V_{10}). The above evolution in morphology indicates that a splitting growth mechanism is most likely responsible, which is observed in the case of Bi_2S_3 growth[20]. It is also noted that some granules appear in V_{10}, indicating a weak long-range order, which is in good accordance with the XRD results.

A TEM characterization of V_{25} was performed to study the crystal structure of Mn_2O_3. Figure 3a clearly shows that the V_{25} sample has a dumbbell structure with a size of approximately 3 μm. The indexing of the selected area electron diffraction (SAED) pattern shown in Figure 3b suggests that each dumbbell is a Mn_2O_3 single crystal structure. In combination with the size of the particle and the single crystal characteristics, it is inferred that the sample is a mesocrystal. After ultrasonic treatment, it can be seen that the particles of the sample are composed of small granules with visible gaps in between particles (Figure 3c). This further confirms that the dumbbell-shaped Mn_2O_3 has a mesocrystal structure. Figure 3d shows a perfect crystal structure within each constituent particle, indicating the long-range order of its crystal structure. From the above analysis, it is concluded that the dumbbells can be formed by the orderly stacking of nanocrystallites.

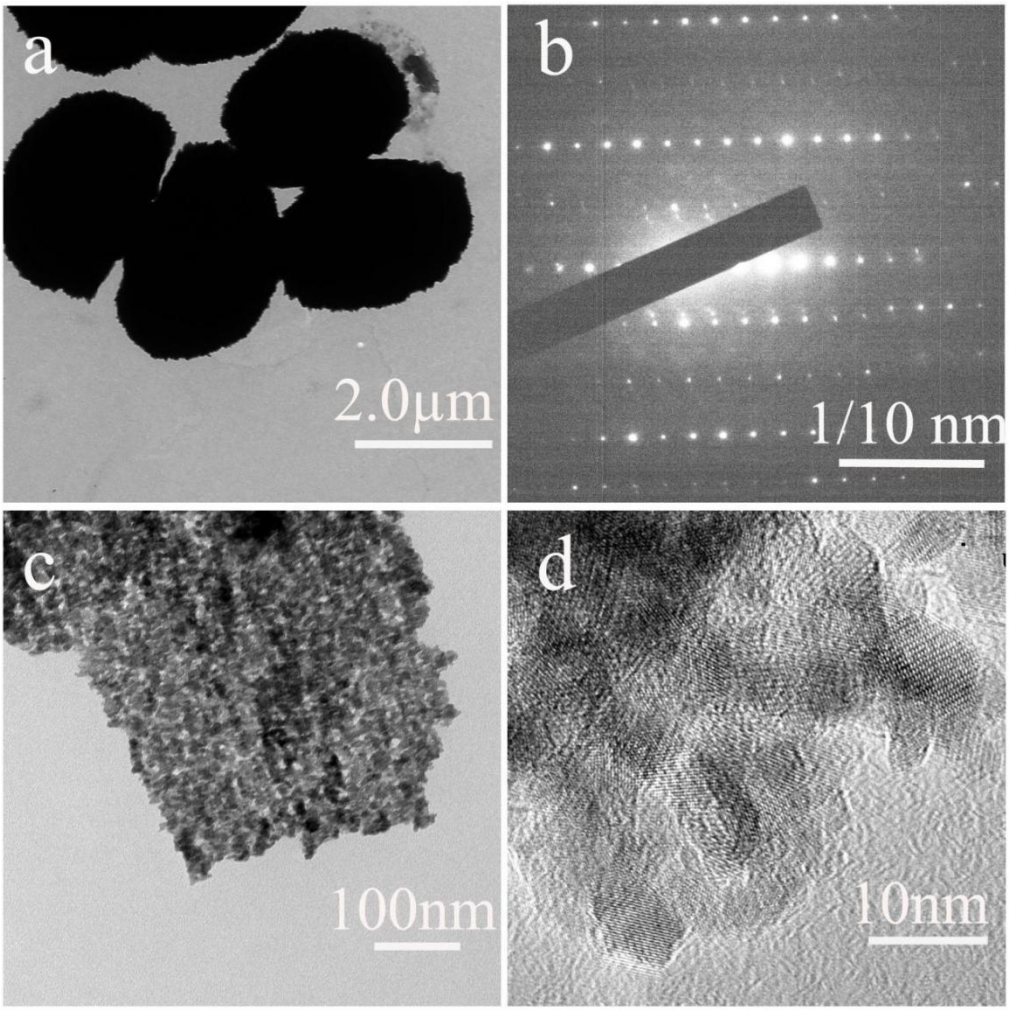

Figure 3. a) TEM image, b) SAED pattern, c) HRTEM, and (d) FFT images of V_{25}.

A large surface area and favourable pore size distribution are known as significant factors in advanced supercapacitor electrode materials. Herein, N_2 adsorption and desorption isotherms of V_{25} and V_{50} were measured to evaluate the surface area of the Mn_2O_3 samples. It can be observed from the figure that the pore structure can hardly be found in the V_{50} sample, while the V_{25} sample shows type-III N_2-adsorption isotherms with H4 hysteresis loops. The above result indicates that the pores are formed due to the aggregation of small particles. This is consistent with the TEM images. The surface area is calculated by the general BET method, and the values are 4.0 and 125.7 cm^2 g^{-1} for V_{50} and V_{25}, respectively.

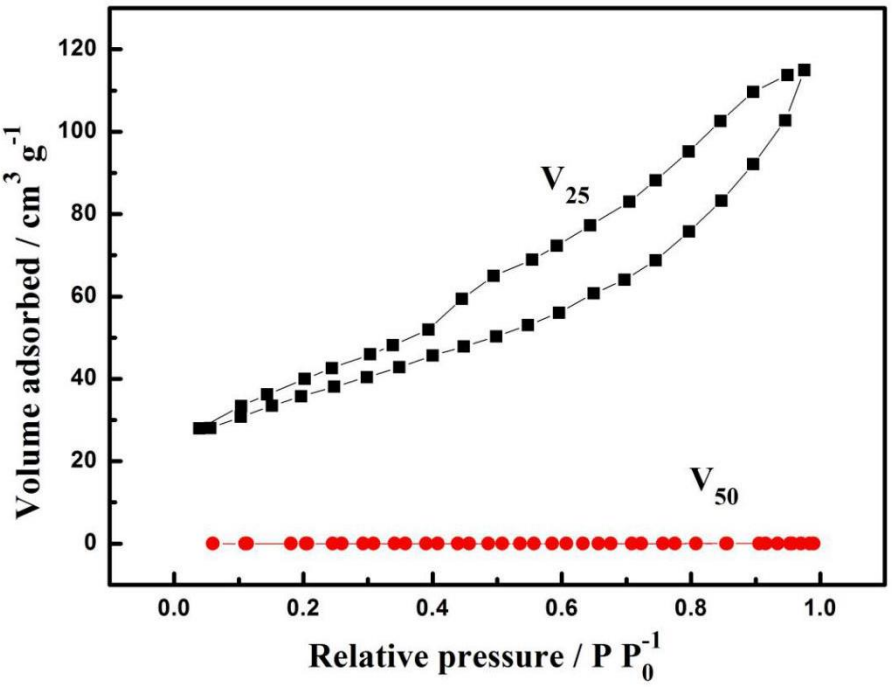

Figure 4. N_2 adsorption and desorption isotherms of V_{25} and V_{50}.

3.2 Electrochemical studies

Figure 5a shows the specific capacitance of the V_{50}~V_{10} samples. It can be seen that with the increase in the water to ethanol ratio, the specific capacitances of the samples first increase from 157.8 F g^{-1} (V_{50}) to 273.1 F g^{-1} (V_{25}) and then decrease to 163.0 F g^{-1} (V_{10}). V_{25} exhibits the highest value. The specific capacitance of the V_{25} sample after 1000 cycles is also presented in Figure 5a, from which it can be seen that V_{25} has good electrochemical cycling stability. The capacitance retention of V_{25} is as high as 97.7% after 1000 cycles. Compared with most of the pure Mn_2O_3 samples(The details are listed in a table1), such as Mn_2O_3 particles[21], Mn_2O_3 nanobar[22], Mn_2O_3 nanofiber[23], Mn_2O_3 nanosperes, Mn_2O_3 nanocubes[24], Mn_2O_3 nanowalls[25], the values reported here are much higher. Figure 5b shows CV curves of the V_{25} sample at various scanning rates. All the curves exhibit good quasi-rectangular characteristics. In particular, the curve still retains good rectangular characteristics even when the scanning rate reaches as high as 200 mV s^{-1}, thus indicating superior capacitance performance. It can be calculated that the specific capacitance of the V_{25} sample at scanning rates of 5, 10, 20, 50, 100 and 200

mV s^{-1} are 290.3, 226.2, 202.1, 157.2, 117.0 and 78.7 F g^{-1}, respectively. The superior capacitance is closely related to the granularity, porosity, large specific surface area and high conductivity of V_{25}, which originates from the connection between the constituent granules.

Table 1 comparison of the electrochemical performance of mesocrystal dumbbell-shaped Mn_2O_3 with other previously reported pure Mn_2O_3 electrodes

Composition	Mass loading (mg cm^{-2})	electrolyte	Capacitance (F g^{-1})	Current density (A g^{-1})	cycles	retention	Ref.
Mn_2O_3 particles	thin films(<1)	Na_2SO_4	84	1	-	-	[21]
Mn_2O_3 nanobar	2	KOH	249.7	0.2	1000	88%	[22]
Mn_2O_3 nanofiber	-	KOH	216	0.5	1000	93%	[23]
Mn_2O_3 nanosperes	1.5	$LiNO_3$	261	1	-	-	[24]
Mn_2O_3 nanocubes	1.5	$LiNO_3$	230	1	-	-	
Mn_2O_3 nanowalls	thin films(<1)	KOH	461	0.5	5000	80%	[25]
dumbbell-shaped Mn_2O_3	3	KOH	273.1	1	1000	97.7%	This work

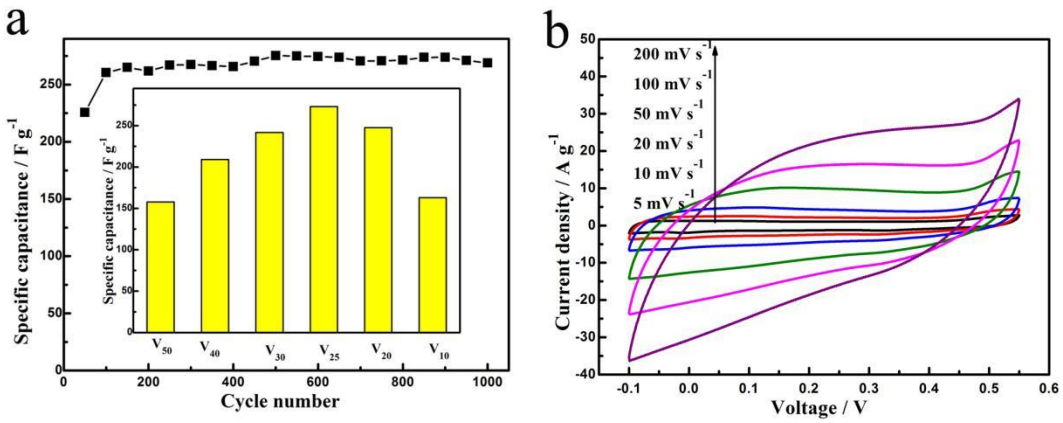

Figure 5. a) Discharge cycle values of V_{25} at 1 A g^{-1} (the inset image is the specific capacitance of different samples at 1 A g^{-1} with voltages ranging from -0.1V to 0.55V) and b) CV curves of the V_{25} sample at various scanning rates in 6 M KOH solution.

To further analyse the capacitance characteristics of the sample materials, the total specific capacitance is divided into the noninsertion capacity and insertion capacity. The former can be represented by the minimum capacitance depending on the scan rate, and the latter is the difference between the maximum capacitance and the minimum capacitance, which is related to the square root of

the scan rate [26]. We plotted the inverse of the capacitance versus the square root of the scan rate for the V_{25} sample in Figure 6 a-b. From Figure 6a, we obtain the total maximum capacitance as 411.5 F g^{-1}, and from Figure 6b, the minimum capacitance is calculated to be 230.5 F g^{-1}.

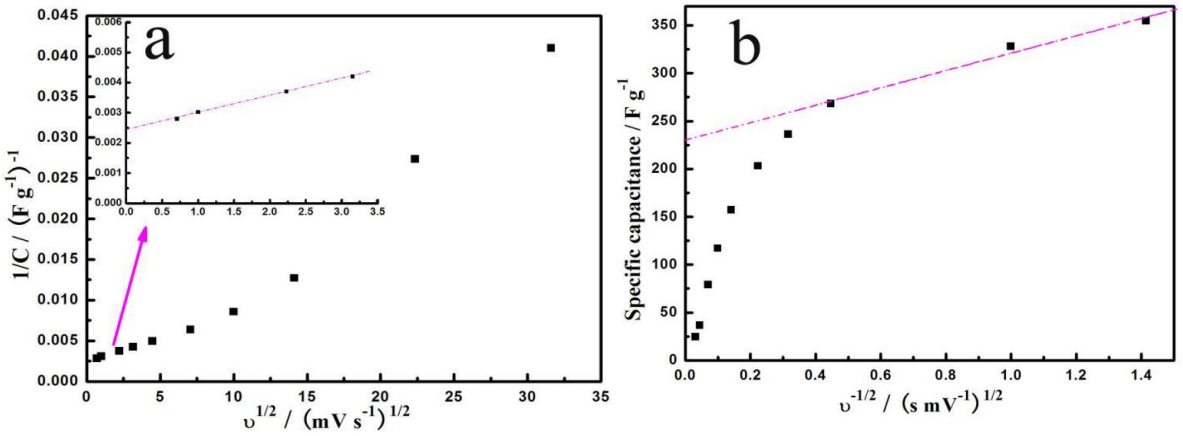

Figure 6. a) 1/C~$v^{1/2}$ and b) C~$v^{-1/2}$ curves of V_{25} （voltages ranging from -0.1V to 0.55V in 6 M KOH）

From the above data, it can be calculated that the insertion capacity percentage is 44%. Compared with that for MnO_2, the total capacitance share of the insertion capacity of Mn_2O_3 materials is much higher. Therefore, in addition to increasing the specific surface area and introducing conductive materials, the capacitance performance of Mn_2O_3 materials can also be improved by optimizing their crystal structure. Moreover, unlike MnO_2, which can only be prepared under low temperature, Mn_2O_3 can stay stable under high temperatures, offering more chance for Mn_2O_3 to bond with additives. The above advantages of Mn_2O_3 over MnO_2 provide it with increased research potential as supercapacitor materials.

4. CONCLUSION

In summary, we successfully prepared mesocrystal dumbbell-shaped Mn_2O_3 by annealing hydrothermal products of $MnCO_3$ and precisely controlling the ratio of water to ethanol. When the ratio of ethanol increased, various Mn_2O_3 nanostructures with different morphologies, ranging from dumbbell-like shape (1:1) to spherical (1:4), were obtained and indicated a splitting growth mechanism. With an increase in the ratio of water to ethanol, the specific capacitance of Mn_2O_3 increased from 157.8 F g^{-1} (V_{50}) to 273.1 F g^{-1} (V_{25}) at a current density of 1 A g^{-1} in 6 M KOH electrolyte and then decreased to 163.0 F g^{-1} (V_{10}). Clearly, Mn_2O_3 (V_{25}) exhibited the highest value, which benefited from its granularity, porosity, large specific surface area and high conductivity. Moreover, Mn_2O_3 (V_{25}) also showed a good capacitance retention of 97.7% after 1000 cycles. Additionally, the noninsertion capacity and insertion capacity of the samples were further discussed to analyse the capacitance characteristics

of Mn_2O_3. The total maximum capacitance and the minimum capacitance were calculated as 411.5 F g^{-1} and 230.5 F g^{-1}, respectively. This work provides new innovative ideas to improve the capacitance performance of Mn_2O_3 material by optimizing the crystal structure, and the results exhibit a promising electrode material for large-scale supercapacitor applications.

ACKNOWLEDGMENTS
We are grateful for the financial support from the Natural Science Projects of Anhui Province (1908085QB84), the Science and Technology Major Project of Anhui Province (18030901087) and the National Natural Science Foundation of China (51904077).

References

1. B.E. Conway, Electrochemical Supercapacitors Scientific Fundamentals and Technological Applications. Kluwer Academic/plenum, New York (1999).
2. M. Zhou, H. Chai, D. Jia and W. Zhou. *New J. Chem*., 38 (2014) 2320.
3. W. Yang, W. Yang, L. Kong, X. Qin and G. Shao. *Carbon*, 127 (2018) 557.
4. M. Toupin, T. Brousse, D. Belanger, *Chem. Mater.,* 16 (2004) 3184.
5. M. Moalleminejad and D. D. L. Chung. *Carbon*, 91 (2015) 76.
6. D. Yan, Y. Li and Y. Liu. *Electrochim Acta*, 169 (2015) 317.
7. A. Subagio, Y. A. Hakim, M. W. Ristiawan, M. A. Kholil, Priyono. *Int. J. Electrochem. Sci.*, 14 (2019) 9936.
8. T. G. Yun, B. Hwang and D. Kim. *ACS Appl. Mater. Interfaces,* 7 (2015) 9228.
9. J. Chen, Y. Liu, G. Wang, J. Guo and X. Wang. *ACS Sustain. Chem. Eng.*, 5 (2016) 1594.
10. C. Yin, H. and Zhou, J. Li. *Ionics,* 25 (2019) 285.
11. E. Lee, T. Lee and B. S. Kim. *J. Power Sources*, 255 (2014) 335.
12. W. Li, J. Shao, Q. Liu, X. Liu, X. Zhou and J. Hu. *Electrochim Acta*, 157 (2015) 108.
13. Z. Li, M. Akhtar,T.M. Bui and O. Yang. *Chem. Eng. J*., 330 (2017) 1240.
14. H. Cölfen and M. Antonietti. *Angew. Chem. Int. Ed*., 44 (2005) 5576.
15. W. Bi, Z. Hu, C. Wu, J. Wu, Y. Wu and Y. Xie. *Nano Res.*, 8 (2015) 193.
16. M. Ma and H. Cölfen. *Curr. Opin. Colloid. In.*, 19 (2014) 56.
17. S. Yang, X. Song, P. Zhang, J. Sun and L. Gao. *Small*, 10 (2014) 2270.
18. W. Bi, Z. Hu, X. Li and C. Wu. *Nano Res.*, 8 (2015) 193.
19. L. Hou, C. Yuan and X. Zhang. *CrysEngComm.*, 13 (2011) 6130.
20. J. Tang and A.P. Alivisatos. *Nano Letters*, 6 (2006) 2701.
21. B. L. Vijayan, I. I. Misnon, G. M. Kumar, K. Miyajima and R. Jose. *J. Colloid Interf. Sci*., 562 (2020) 567.
22. S. Maiti, A. Pramanik and S. Mahanty. *CrystEngComm.*, 18 (2016) 450.
23. J. Liang, L. Bu, W. Cao, T. Chen and Y. Cao. J. Taiwan Inst. Chem. Eng., 65 (2016) 584.
24. S. Alagar, R. Madhuvilakku, R. Mariapan and S. Piraman. *J. Power Sources,* 441 (2019) 227181.
25. Z. Y. Li， M.S. Akhitar, P.T.M. Bui, O. B. Yang. *Chem. Eng. J,* 330 (2017) 1240.
26. T. Brezesinski , J. Wang, J. Polleux , B. Dunn and S.H. Tolbert . *J. Am. Chem. Soc.*, 131 (2009) 1802.